A&A 436, 601–606 (2005)
DOI: 10.1051/0004-6361:20042477

Astronomy & Astrophysics

High resolution *H* band imaging polarimetry of IRC +10216

The obscured location of the central star

K. Murakawa[1,⋆], H. Suto[1], S. Oya[1], J. A. Yates[2], T. Ueta[3,⋆⋆], and M. Meixner[4]

[1] Subaru Telescope, 650 North A'ohoku place, Hilo, HI 96720, USA
e-mail: murakawa@naoj.org
[2] University College London, Gower street, London, WC1E 6BT, UK
[3] Royal Observatory of Belgium, Ringlaan 3, 1180 Brusseles, Belgium
[4] Space Telescope Science Institute, 3700 San Martin Drive, Baltimore, MD 21282, USA

Received 30 August 2004 / Accepted 3 February 2005

Abstract. We have carried out an *H* band imaging polarimetry of an evolved AGB star IRC +10216 using CIAO and AO on the Subaru telescope. Our polarimetric images show NE-S bipolar lobes, a NW lobe, a discrete NW arc with ∼4.″2 radius and two new features of a fan-like shape at the SE and of an elliptic shape at the NW with small polarizations ($P < 4\%$) near the intensity peak. The polarization vectors in the NE-S lobes and the NW lobe have a centrosymmetric pattern centered at the position of the illumination source (the central star). The illumination source is located at (+0.″25, −0.″065) from the intensity peak between the SE fan and the NW ellipse. The polarization vectors between these two features are aligned along a line across them. We interpret that the appearance of the SE fan and the NW ellipse reflects a sudden increase of the mass loss rate that likely initiated the formation of an edge-on dust torus. This sudden mass loss increase probably began about a half century ago.

Key words. infrared: stars – stars: individual: IRC +10216 – techniques: polarimetric – circumstellar matter

1. Introduction

IRC +10216 (CW Leo) is the best studied C-rich evolved star. It is thought to be in transition from an asymptotic giant branch star (AGB) to a proto-planetary nebula (PPN). Previous imaging at various spatial scales revealed spatial variations of surface brightness in the circumstellar envelope (CSE). Mauron & Huggins (1999, 2000) and Mauron et al. (2003) showed that discrete spherical shells of dust were seen by scattering of ambient Galactic light in >1′ scale. A similar morphology was also detected in CO gaseous emission (Fong et al. 2003). Kastner & Weintraub (1994) presented near-infrared polarimetric images using a coronagraph. The polarimetric signature indicated that a N-S bipolar reflection nebula extending ∼10″ was seen due to scattering of light from the central star by dust particles in the nebula. Skinner et al. (1998) estimated using an HST WFPC2 image that an asymmetric feature started to appear about 250 years ago. Recent development in high resolution imaging techniques with 5−10 m class telescopes has allowed us to image with sub-0.″1 angular resolution exceeding the constraint imposed by natural seeing. Weigelt et al. (1998) have monitored IRC +10216 in the near-infrared using a bispectrum technique since 1995 (see also Weigelt et al. 2002; Osterbart et al. 2000). They have identified four major clumps within 0.″5 scale at the S, N, E, and W of the "center" of the nebula (respectively labeled as clump A, B, C, and D). Their multi-epoch images since 1995 have shown an interesting time-sequence as to how a circumstellar environment close to an evolved star behaves (Weigelt et al. 2002).

The CSE morphology is known to vary in different evolutionary phases. For example, near spherical distribution of H_2O maser spots has been detected in Mira variables (e.g. Bains et al. 2003). A bipolar structure with several concentric arcs has been seen in PPNs (e.g. Hrivnak et al. 2001). A clear bipolar or multi-polar structure has often been seen in PNs (e.g. Corradi et al. 1995). Morphological variations of the CSEs are often seen in different spatial scales as in the case of IRC +10216 described above. These results represent strong evidence suggesting that mass loss progresses from near isotropy to anisotropy in the late stellar evolutionary phases. Meixner et al. (1999) and Ueta et al. (2000) have surveyed a large number of evolved stars in the mid-infrared and optical. They have concluded that PPNs are intrinsically axisymmetric due to equatorially enhanced (toroidal) distribution of dust grains in the shell. Such structures may be formed by a "superwind", which is a sudden increase of mass loss to

⋆ *Present address*: Max-Planck-Institut für Radioastronomie, Auf dem Hügel 69, 53121 Bonn, Germany.
⋆⋆ *Present address*: NASA Ames Research Center/SOFIA, MS 211-3, Moffett Field, CA 94035-1000, USA.

remove almost the entire remaining hydrogen-rich surface layer of the star, and terminates the AGB evolution (Renzini 1981; Iben & Renzini 1983). This superwind mechanism appears to create the axisymmetric morphology starting in the evolved AGB phase and the early PPN phase.

In order to study how the morphology of the CSEs changes from spherical to axisymmetric during the late evolutionary phases, we have carried out high resolution imaging polarimetry of IRC +10216. Polarimetry is a powerful technique to investigate the illumination source, geometry of the CSEs, and dust properties (shape, alignment and size distribution of grains). Gledhill et al. (2001); Su et al. (2003); Ueta et al. (2005) have successfully revealed axisymmetric features of the CSEs using near-infrared imaging polarimetry. We have used this technique to directly detect the dust torus around an evolved AGB star and to confirm that the polarimetry is an excellent technique for understanding the geometry of dust envelope around the star.

2. Observations and results

2.1. Observation

We obtained polarimetric images of IRC +10216 in the *H* band on 2003 January 3 using a near-infrared high resolution camera named the Coronagraphic Imager with Adaptive Optics (CIAO; Murakawa et al. 2004) and the 36-element adaptive optics (AO; Takami et al. 2003) system mounted on the 8 m Subaru telescope. CIAO employs a rotatable half wave plate (HWP) installed in front of the AO optics and a fixed wire grid polarizer in the cryostat to measure the linear polarization. The natural seeing was about 0.″6 at *R* band, and the sky conditions were stable during the observation. Since there is no appropriate single star near the object, we used the object itself as an AO guide star even though it has an extended nebulosity and is faint (∼15 mag) at *R* band (the wavelength for wave front sensing). Thus, the point-spread function (PSF) did not achieve the diffraction-limit of ∼0.″06 at *H* band. The full width at half maximum (*FWHM*) was estimated to be about 0.″25 (see also Fig. 8 in Oya et al. 2004). Thus, we used a medium resolution camera with 0.0217 arcsec pix^{-1} pixel scale (22″ × 22″ FOV).

We used a narrow *Hcont* band filter (λ_c = 1.573 μm, $\Delta\lambda$ = 0.02 μm) instead of a broad *H* band filter (λ_c = 1.65 μm, $\Delta\lambda$ = 0.3 μm) to avoid saturation of the array output signal level. Three-point dither with 1″ separation was applied to remove bad pixels. At each dither position, we obtained four sets of images ($I_{0.0}$, $I_{45.0}$, $I_{22.5}$, and $I_{67.5}$) by rotating the HWP with position angles (PAs) of 0, 45.0, 22.5 and 67.5°, respectively, and repeated this process four times. The exposure time per image acquisition was 0.5 s. One frame consists of 10 co-added images. We obtained 24 frames per HWP PA per dither position. The total integration time for the total intensity (the Stokes *I*) was, therefore, 24 min.

2.2. Data reduction

We reduced the data using our own command language (cl) scripts on the image reduction and analysis facility (IRAF). First, the dark frame was subtracted from each object frame. The flat fielding was done with the dome flat, and bad pixels were removed. The flux centroid of the object image in each frame was used to estimate the position accuracy. The error was 0.33 pixels (∼7 mas). This value is reasonable in AO imaging because the AO Tip/Tilt correction stabilizes the position of the object. Hence, we considered that the contribution of the position uncertainty of ∼7 mas would be negligible in combining images. However, the temporal variation of the wave front in higher order components remained even after the AO correction and was the dominant error source in the final images. All frames for each HWP position were then combined into 12 images. All images at each dither positions were aligned with the position of the object determined using the flux centroid. We finally obtained four averaged images of $I_{0.0}$, $I_{45.0}$, $I_{22.5}$ and $I_{67.5}$ and their standard deviation. The signal-to-noise ratio (SNR) at each pixel around the intensity peak was found to be ∼100.

The Stokes *IQU* parameters were calculated from these 4 images using a matrix $\boldsymbol{M}$ defined as $(I, Q, U) = \boldsymbol{M}(I_{0.0}, I_{22.5}, I_{45.0}, I_{67.5})$. The equations we followed to reduce the polarimetric data are presented in Appendix A. The matrix $\boldsymbol{M}$ is a function of the total intensity transmission T of both the HWP and the wire grid polarizer, and the efficiency η of the wire grid polarizer. Since the efficiency of the HWP was almost 1 within the measurement error of 1%, we assumed 100% efficiency for the HWP. The measured transmission T and the efficiency η using a calibration polarizer and the dome flat lamp are 0.402 and 0.875 at *H* band, respectively. From the calibration data, we determined the measurement errors in the degree of linear polarization σ_P and in the polarization angle σ_θ to be <1% and <±1°, respectively. The instrumental θ_o offset was estimated to be 4.8°. The polarized flux (I_P), the degree of the linear polarization (P), and the orientation of polarization (θ) were derived from these Stokes *IQU* parameters.

We also analyzed errors of the Stokes *IQU* parameters and of I_P, P and θ. We followed the algorithm presented by Sparks & Axon (1999). Since this algorithm is designed for the HST NICMOS three-element polarizer, we used a modified four-element version of the algorithm to analyze our data. The algorithm of the error propagation is presented in Appendix A. Typical errors of σ_P and σ_θ are respectively <3% and <15° per pixel within 2″ from the intensity peak. Although σ_θ may be somewhat large, binning with several pixels improved the signal-to-noise ratio and helped in reducing σ_θ. The final error will be presented in Sects. 2.3 and 3.1.

2.3. Polarimetric image

Figure 1a shows the total intensity I map on the negative logarithmic gray scale with polarization vectors. The FOV is 10″ × 10″. The vector lines are drawn every 12 pixels (∼0.″25). Between ∼0.″5 and ∼2″ from the intensity peak, the polarization vectors show a centrosymmetric pattern surrounding the intensity peak. In our *H* band image, we do not recognize the elliptical vector pattern with the major axis in the direction of E-W presented in the previous *J* band polarimetric image by Kastner & Weintraub (1994). In spite of mostly symmetric

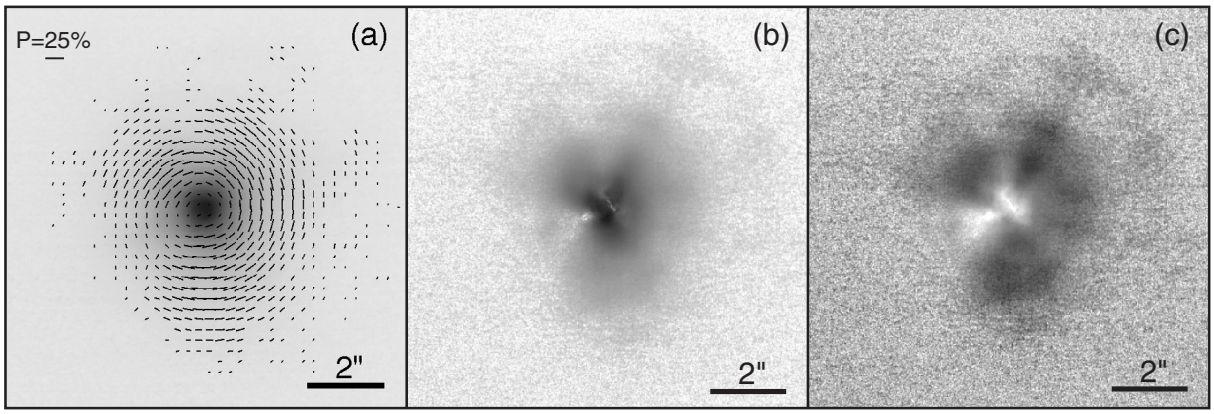

Fig. 1. a) The total intensity I with polarization vectors, **b)** the polarized flux I_P, and **c)** the degree of the linear polarization P. North is up and east to the left in these images. The FOV is $10'' \times 10''$ in each image. The gray scale in **a)** and **b)** are on the logarithmic and all figures are on the negative scale. The vector lines in **a)** are drawn every 12 pixels (~0.″25). **a)** Shows a spherical nebulosity, and a typical centrosymmetric pattern surrounding the intensity peak. Polarimetric images **b)** and **c)** show a NE-S bipolar, a NW-radial structure and an arc with ~4.″2 radius from the northeast to the west via the northwest. These features have polarizations of 15−24%. There are a fan-like feature and an ellipse feature each with small polarizations ($P < 4\%$) within ~0.″5 from the center.

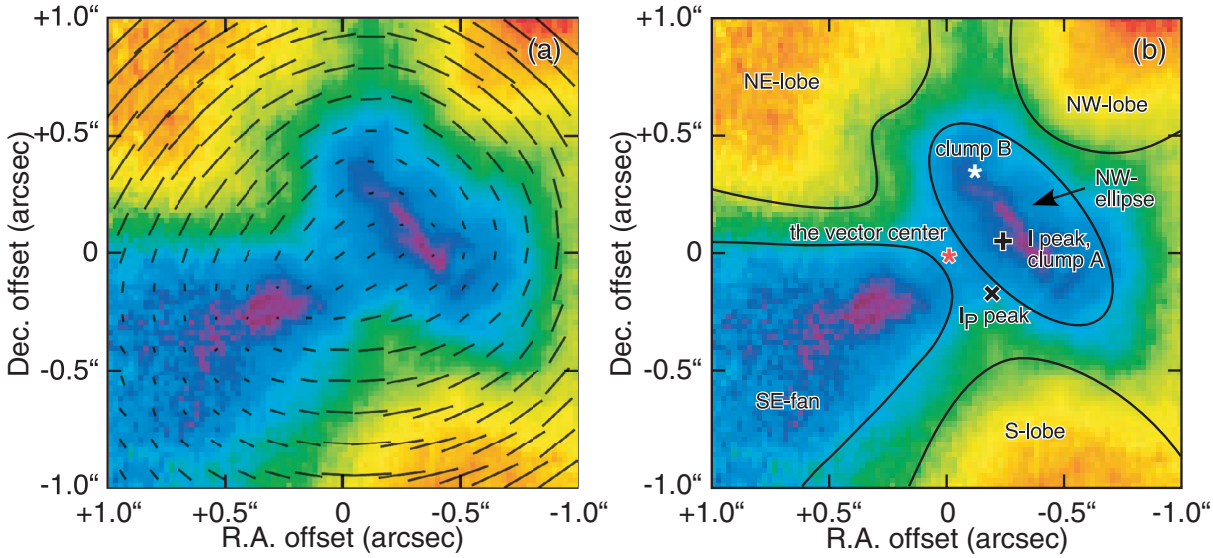

Fig. 2. The central $2'' \times 2''$ FOV of Fig. 1c is magnified **a)**. North is up and east to the left. The violet, blue, green, yellow, and red denote degree of polarizations of ~0%, a few percent to 5%, ~10%, 15−20%, and 20−25%, respectively. The polarization vector lines are drawn each 6 pixels (~0.″13). **b)** Explains features seen in **a)**. A fan-like feature and an elliptic feature with small polarization ($P < 4\%$) are seen. The peak positions of the total intensity and the polarized flux are presented with + and x, respectively. The center of the centrosymmetric vector pattern as the position of the star, derived from the polarization vectors at the NE, S and NW lobes, is indicated by a red asterisk. The position offset from the intensity peak is (+0.″25, −0.″065) with its error of 0.″03. As a comparison, the position of the clump B at the epoch 2001 (Weigelt et al. 2002) is also indicated by a white asterisk. Osterbart et al. (2000) and Men'shchikov et al. (2001, 2002) have predicted that the star IRC +10216 exists at or near the clump B.

appearance of the I map, the I_P and P maps (Figs. 1b and 1c, respectively) show some asymmetry. There are two lobes extending towards the NE and S, another lobe extending towards the NW, and an arc-like feature with ~4.″2 radius from the NE to the W. These features are also seen in previous images with middle-size FOVs (e.g. Kastner & Weintraub 1994; Skinner et al. 1998; Murakawa et al. 2002). The NE and S lobes have polarizations of 15−20%, and the NW lobe has 15−24%. In Fig. 1c, we identify two new features with small polarizations ($P < 4\%$) around the intensity peak. One has a fan-like shape at the SE with an opening angle of 59°. The other has an elliptical shape at the NW with the 0.″8 major axis (of 43° PA) and the 0.″5 minor axis (see also Fig. 2b).

We show in Fig. 2 the central $2'' \times 2''$ field of the Fig. 1c. The pseudo color denotes the degree of linear polarization. The polarization vector lines are drawn every six pixels (~0.″13). The σ_θ is about 1° to 2° in a 6×6 binned box in these two regions of small P. Therefore, the polarization vectors between the two low polarization features are aligned with a line (of ~125° PA) across the SE fan and the NW ellipse. Figure 2b describes the features seen in the P map. The peak positions of the intensity and the polarized flux are presented with +

and x, respectively. The details of two asterisks will be explained in Sect. 3.1.

The unpolarized component of the central star light can dilute the degree of polarization in the reflection nebula near the star. This effect is often seen in objects with a bright central star with an optically thin reflection nebula such as PPNs and details are discussed by Gledhill et al. (2001) and Ueta et al. (2005). IRC +10216 is, however, deeply embedded in a thick dust envelope. The optical depth at the *H* band is as high as 7 (Men'shchikov et al. 2001) and the central star is invisible. The unpolarized PSF component is not expected to be strong enough to change the polarization characteristics of the object. That does not affect our interpretation of the polarimetric image in Fig. 2b including that of the asymmetric features.

3. Discussion

3.1. The position of the central star

We have analyzed our polarimetric data to identify the position of the central star. We used polarization vectors showing a general centrosymmetric pattern in the regions with sufficiently high SNRs in the degree of polarization. The position of the illumination source can be traced backwardly from each polarization vector. The center of the centrosymmetric pattern was determined by minimizing the sum of the square of the distance from the presumed center to a line orthogonal to the polarization vectors. The algorithm of this analysis is presented in Appendix B. We selected three regions in the NE, S and NW lobes that are 0.″5 to 1.″6 away from the intensity peak. The 4×4 binning was applied because in each binned box the σ_θ error becomes comparable with the angular variation of the polarization vectors in the centrosymmetric pattern ($\sim 2^\circ$). The estimated position of the central star is off by (+0.″25, −0.″065) from the intensity peak with the position error of 0.″03. This error is comparable with σ_θ and variation of θ in each binned box. Note that the position accuracy of ∼7 mas (see Sect. 2.2) is much smaller than the position error (0.″03) and thus does not affect our result. Therefore, we can pinpoint the position of the central star: it is located between the SE fan and the NW ellipse, and is indicated by a red asterisk in Fig. 2b.

IRC +10216 is deeply embedded in a dust shell, and therefore, it has been difficult to accurately determine the position of the central star. Prior to the observation by Osterbart et al. (2000), the central star was suggested to be located in the bright southern peak (the clump A). Osterbart et al. (2000) compared their *H* band speckle images obtained on January 1997 with HST NICMOS polarimetric data at 1.1 μm obtained on April 30, 1997, to identify the position of the central star. In the *H* band speckle data, the degree of the linear polarization at the clump A was found to be ∼14% and the polarization vectors did not indicate the center in the clump A. These results would favor that the clump A is caused by scattered light. The polarization vectors in the NICMOS data indicated that the center of the polarization pattern is located in the clump B or a position between the clumps A and B. Men'shchikov et al. (2001, 2002) have performed two-dimensional (2D) radiative transfer modeling taking into account various parameters (such as the luminosity of the central star, the effective stellar temperature, the dust shell geometry and its density distribution, dust grain chemistry and size distribution, and viewing angle). Their model suggested that the position of the clump B would be the most likely location of the central star.

We now compare our polarimetric data with *H* band speckle data in March 2001, the closest date to our observations (the middle panel of Fig. 2 in Weigelt et al. 2002). The appearance of the dust shell of IRC +10216 has changed. Osterbart et al. (2000) measured proper motions of the four clumps in the *K* band. Although the appearance of the thick dust shell is expected to wildly vary in wavelength, Weigelt et al. (2002) pointed out that *H* band images show similar clumpiness to *K* band images. Therefore, we can use the *K* band proper motion to project the *H* band proper motion. The apparent separation between the clump A and B has increased at the velocity of 28 mas yr^{-1} with an acceleration of ∼3−5 mas yr^{-1} (Weigelt et al. 2002; Tuthill et al. 2000). There is 22-month time difference between our observations and the observations by Weigelt et al. (2002). Thus, the separation between the clumps A and B is expected to be about 60 mas. The predicted position of the clump B is (+0.″14, +0.″35) away from the clump A and is indicated with a white asterisk in Fig. 2b. Assuming that the clump A in the speckle image coincides with the intensity peak in our image, the projected position of the clump is off by (+0.″11, −0.″42) with respect to the center of the centrosymmetric pattern, i.e. the location of the central star. The spatial resolution of our image (*FWHM* ∼ 0.″25) is different from that of the speckle image (56 mas resolution). The position uncertainty in the image alignment with different resolution is expected. Therefore, it is difficult to explain the separation between the location of the central star in our results and the predicted position of the central star (the clump B) by the position uncertainty of our data. Thus, the central star does not appear to be located in the clump B.

3.2. Dust torus

We interpret the appearance of the SE fan and NW ellipse seen in Fig. 2 as a near edge-on dust torus surrounding the central star. These features would indicate the both edges of the torus. The equatorial plane of the torus lies on a line across the SE fan and the NW ellipse. Previous sub-arcsec scale images revealed a "dark lane" in the E-W direction, and the existence of a disk or torus like structure was suggested in the dark lane (Dyck et al. 1984; Skinner et al. 1998; Tuthill et al. 2000). Our result is in good agreement with the previous results. Bipolar cavity structure is hinted by the regions with slightly larger polarizations ($P \sim 10\%$) near the predicted star position at the NE and S. The cavity wall may be responsible to somewhat centrosymmetric polarization vector pattern. The peak of the polarized flux is located in the southern cavity. This would suggest that the southern cavity points toward us. That was also predicted with a radiative transfer modeling by Men'shchikov et al. (2001, 2002). A high polarization ($P \sim 15-24\%$) in the NW radial feature can be explained by illumination with light leaking through gaps that exist somewhere in the NW side

of the torus (i.e. in the NW ellipse). The higher polarization in this region may be due to scattering at angle close to 90°. Such polarization could occur if the direction of the gaps in the NW torus is in the plane of the sky and if the NE and S lobes are slightly inclined from the sky plane due to the orientation of the torus: the S lobe seems to point toward us. Light leaks out of the gaps in the NW part of the torus, while only a small number of photons can escape in the SE part of the torus, which is more dense and does not have any gaps. As a result, small polarization and fan-like distribution of polarized light are possible due to multiple scattering. Although we do not see a clear outer edge of the torus in our polarimetric images, the outer edge of the torus may exist around the region with the local polarization minimum: the radius is expected to be ∼0.″5−1.″0.

IRC +10216 is thought to be in a very advanced stage in the AGB phase because of its long luminosity period of ∼650 days (e.g. Le Bertre 1992) and a large mass loss rate of $\sim 2 \times 10^{-5}\ M_\odot\ \mathrm{yr}^{-1}$ (Ivezić & Elitzur 1996; Danchi et al. 1994). Stars at this phase are expected to experience a sudden increase in mass loss rate (e.g. 10^{-8}−$10^{-6}\ M_\odot\ \mathrm{yr}^{-1}$ to $10^{-4}\ M_\odot\ \mathrm{yr}^{-1}$ Blöcker 1995). The degree of the linear polarization has dramatically changed in the two new features of SE fan and the NW ellipse. This is likely resulted from a rapid increase of dust density, which might be related to an extreme mass loss event. If such an extreme mass loss took place, it would have happened about a half century ago assuming the expansion velocity of ∼15 km s^{-1} in gas-phase molecules (e.g. Solomon et al. 1971) and the distance of ∼100−150 pc (Zuckerman et al. 1986; Kastner 1992; Groenewegen et al. 1998).

4. Conclusions

We have performed an *H* band imaging polarimetry of an evolved AGB star IRC +10216 using CIAO and AO on the Subaru telescope. The spatial resolution acheived was about 0.″25. We have derived the Stokes *IQU* parameters, from which we have derived the polarized flux (I_P), the degree of the linear polarization (P), and the polarization position angle (θ) along with their errors. The errors in the degree of linear polarization σ_P and in the polarization position angle σ_θ are respectively 3% and 15° per pixel.

The Stokes *I* image shows mostly symmetric appearance, while the I_P map and the *P* map reveal NE-S bipolar lobes, a NW lobe, and an arc-like feature at the NW. Our polarimetric images also reveal (1) two new features of a fan-like shape at the SE and an elliptic shape at the NW with small polarizations (<4%) near the intensity peak; (2) a centrosymmetric polarization vector pattern in the bipolar lobes; and (3) aligned polarization vectors in the two new features with the PA of ∼125°. We have determined the position of the central star by pinpointing the location of the illumination source in the reflection nebula using the polarization vectors. The position of the central star is off by (+0.″25, −0.″065) from the position of the total intensity peak. Our data suggest that the location of the central star is between the SE fan and the NW ellipse, which is off by (+0.″11, −0.″42) from the predicted position of the moving clump B, in which the central star was thought to reside in the previous studies (Osterbart et al. 2000; Men'shchikov et al. 2001, 2002).

We interprete that the SE fan and the NW ellipse are the two sides of a near edge-on dust torus of 0.″5−1″ radius based on the polarization characteristics of these structures and the surrounding area. It is likely that a sudden decrease of the degree of polarization is due to a sudden increase of dust density. Taking into account the expansion velocity of $v_\mathrm{exp} \sim 15$ km s^{-1} and the distance of ∼100−150 pc, the dusty torus seems to have begun to form about a half century ago.

Appendix A: Polarimetric data analysis

The Stokes *IQU* parameters are derived from 4 images of $I_{0.0}$, $I_{22.5}$, $I_{45.0}$, and $I_{67.5}$ using a matrix $\boldsymbol{M}$ as;

$$\begin{pmatrix} I \\ Q \\ U \end{pmatrix} = \boldsymbol{M} \begin{pmatrix} I_{0.0} \\ I_{22.5} \\ I_{45.0} \\ I_{67.5} \end{pmatrix} = \begin{pmatrix} M_{11} & M_{12} & M_{13} & M_{14} \\ M_{21} & M_{22} & M_{23} & M_{24} \\ M_{31} & M_{32} & M_{33} & M_{34} \end{pmatrix} \begin{pmatrix} I_{0.0} \\ I_{22.5} \\ I_{45.0} \\ I_{67.5} \end{pmatrix}.$$

The matrix consists of the total intensity transmission T and the efficiency of the polarizer η and transforms the observed quantities $I_{0.0}$, $I_{22.5}$, $I_{45.0}$, and $I_{67.5}$ to the Stokes *IQU* parameters. After the transformation, the Stokes *IQU* parameters are expresses by the observed quantities as follows:

$$\begin{aligned} I &= \frac{1}{2T}\left(I_{0.0} + I_{22.5} + I_{45.0} + I_{67.5}\right), \\ Q &= \frac{1}{T\eta}\left(I_{0.0} - I_{45.0}\right), \\ U &= \frac{1}{T\eta}\left(I_{22.5} - I_{67.5}\right). \end{aligned} \tag{A.1}$$

The polarized flux I_P, the degree of the linear polarization P and the polarization position angle θ in radian are converted from the *IQU* using the following formulae;

$$I_\mathrm{P} = \sqrt{Q^2 + U^2},\ P = \frac{I_\mathrm{P}}{I},\ \theta = \frac{1}{2}\arctan\left(\frac{U}{Q}\right) - \theta_\mathrm{o}. \tag{A.2}$$

The polarization position angle has an instrumental offset θ_o, which needs to be corrected using calibration data taken from polarimetric standard stars.

The errors of the Stokes *IQU*, the polarized flux, the degree of the linear polarization and the polarization position angle are computed using the algorithm based on the one presented by Sparks & Axon (1999). The errors in the Stokes parameters σ_i (i = 1, 2 and 3, or I, Q and U) are given by;

$$\sigma_i^2 = \sum_{k=1}^{4} \left(M_{ik}\sigma_{I_k}\right)^2,$$

where σ_{I_k} (k = 1, 2, 3 and 4, or 0, 42, 45, 67.5) are the standard deviation for each HWP angle. As shown in Eq. (A.2), P is a function of I, Q and U, all of which have common parameters. They, I and Q, and I and U, have common parameters. Therefore, the covariances between I and Q (σ_{IQ}), and I and U (σ_{IU}) should be taken into account to estimate the σ_P error. They are given by

$$\sigma_{Ij}^2 = \sum_{k=1}^{4} M_{Ik} M_{jk} \sigma_{I_k}^2,$$

Article published by EDP Sciences and available at http://www.edpsciences.org/aa or http://dx.doi.org/10.1051/0004-6361:20042477

where j is Q or U. On the other hand, $I_{\rm P}$ and θ are functions of Q and U, which are independent parameters (see Eq. (A.1)). The covariance σ_{QU} can be ignored in errors of $I_{\rm P}$ and P. We finally obtain the errors of $\sigma_{I_{\rm P}}$, $\sigma_{\rm P}$ and σ_θ (in radian) as below;

$$\sigma^2_{I_{\rm P}} = \frac{1}{I^2_{\rm P}}\left(Q^2\sigma^2_Q + U^2\sigma^2_U\right),$$
$$\sigma^2_{\rm P} = \frac{1}{I^2}\left(\sigma^2_{I_{\rm P}} + P^2\sigma^2_I - 2\frac{Q}{I}\sigma^2_{IQ} - 2\frac{U}{I}\sigma^2_{IU}\right),$$
$$\sigma^2_\theta = \frac{1}{\left(2I^2_{\rm P}\right)^2}\left(U^2\sigma^2_Q + Q^2\sigma^2_U\right).$$

Appendix B: Identification of the position of the central star

Ideally, the position of the illumination source is on a line perpendicular to any polarization vector in the region where a centrosymmetric polarization pattern is seen, i.e. the region where the polarization is resulted from single scattering. However, this will not be the case in reality because of the measurement errors. The position of the illumination source $S\,(x_{\rm s}, y_{\rm s})$ is determined using a least square method described below.

Let x and y be the pixel coordinates on the image. The x-axis is on the negative right ascension and the y-axis is on the positive declination. The polarization position angle θ_i is measured from the N towards the E in counter-clock wise. Let L^2_i be the square of the distance between the position of the illumination source and the line perpendicular to a polarization vector located at $P_i(x_i, y_i)$;

$$L^2_i = \left\{\sin\theta_i\,(x_{\rm s} - x_i) - \cos\theta_i\,(y_{\rm s} - y_i)\right\}^2.$$

If we let L^2 be the sum of all L^2_i (i.e. $L^2 = \sum L^2_i$), then the correct stellar position would be the one which minimizes L^2. The solution should be derived from

$$\frac{\partial L^2}{\partial x_{\rm s}} = 0, \text{ and } \frac{\partial L^2}{\partial y_{\rm s}} = 0.$$

These can be expressed in a matrix form;

$$\begin{pmatrix} x_{\rm s} \\ y_{\rm s} \end{pmatrix} = \boldsymbol{A}^{-1}\boldsymbol{B}, \tag{B.1}$$

where

$$\boldsymbol{A} = \begin{pmatrix} \sum\sin^2\theta_i & -\sum\sin\theta_i\cos\theta_i \\ -\sum\sin\theta_i\cos\theta_i & \sum\cos^2\theta_i \end{pmatrix},$$

$$\boldsymbol{B} = \begin{pmatrix} \sum\sin^2\theta_i x_i - \sum\sin\theta_i\cos\theta_i y_i \\ \sum\cos^2\theta_i y_i - \sum\sin\theta_i\cos\theta_i x_i \end{pmatrix}.$$

The error of the estimated position σ is the square root of L^2 using the estimated position of the central star, $(x_{\rm s}, y_{\rm s})$.

Acknowledgements. Dr. T. Ueta has been partly supported by the project IAP P5/36 financed by FSTC of the Belgian State. We would appreciate the fruitful discussions of the circumstellar envelope around evolved stars with Prof. G. Weigelt, Dr. K. Ohnaka and their research members. We also wish to thank the Subaru Telescope staff for the support and encouragement for our observations.

References

Bains, I., Cohen, R. J., Louridas, A., et al. 2003, MNRAS, 342, 8
Blöcker, T. 1995, A&A, 297, 727
Corradi, R. L. M., & Schwarz, H. E. 1995, A&A, 293, 871
Danchi, W. C., Bester, M., Degiacomi, C. G., et al. 1994, AJ, 107, 1469
Dyck, H. M., Zuckerman, B., Leinert, Ch., & Beckwith, S. 1984, ApJ, 287, 801
Fong, D., Meixner, M., & Shah, R. Y. 2003, ApJ, 582, 39
Gledhill, T. M., Chrisostomou, A., Hough, J. H., & Yates, J. A. 2001, MNRAS, 322, 321
Groenewegen, M. A. T., van der Veen, W. E. C. J., & Matthews, H. E. 1998, A&A, 338, 491
Hrivnak, B. J., Kwok, S., & Su, K. Y. L. 2001, AJ, 121, 2775
Iben, I. Jr., & Renzini, A. 1983, ARA&A, 21, 271
Ivezić, Ź., & Elitzur, M. 1996, MNRAS, 299, 1019
Kastner, J. H. 1992, ApJ, 401, 337
Kastner, J. H., & Weintraub, D. A. 1994, ApJ, 434, 719
Le Bertre, T. 1992, A&AS, 94, 377
Mauron, N., & Huggins, P. J. 1999, A&A, 349, 203
Mauron, N., & Huggins, P. J. 2000, A&A, 359, 707
Mauron, N., de Laverny, P., & Lopez, B. 2003, A&A, 401, 985
Meixner, M., Ueta, T., Dayal, A., et al. 1999, ApJ, 122, 221
Men'shchikov, A. B., Balega, Y., Blöcker, T., Osterbart, R., & Weigelt, G. 2001, A&A, 368, 497
Men'shchikov, A. B., Hofmann, K.-H., & Weigelt, G., 2002, A&A, 392, 921
Murakawa, K., Tamura, M., Suto, H., et al. 2002, A&A, 395, L9
Murakawa, K., Suto, H., Tamura, M., et al. 2004, PASJ, 56, 509
Osterbart, R., Balega, Y. Y., Blöcker, T., Men'shchikov, A. B., & Weigelt, G. 2000, A&A, 357, 169
Oya, S., Takato, N., Takami, H., et al. 2004, Proc. SPIE, 5490, 409
Renzini, A. 1981, in Physical Processes in Red Giants (Dordrecht; Reidel), 431
Skinner, C. J., Meixner, M., & Bobrowsky, M. 1998, MNRAS, 300, 29
Sparks, W., & Axon, D. J. 1999, PASP, 111, 1298
Solomon, P., Jefferts, K. B., Penzias, A. A., & Wilson, R. W. 1971, ApJ, 163, L53
Su, K. Y. L., Hrivnak, B., Kwok, S., & Sahai, R. 2003, ApJ, 126, 848
Takami, H., et al. 2003, Proc. SPIE, 4839-03
Tuthill, P. G., Monnier, J. D., Danchi, W. C., & Lopez, B. 2000, ApJ, 543, 284
Ueta, T., Meixner, M., & Bobrowsky, M. 2000, ApJ, 528, 861
Ueta, T., Murakawa, K., & Meixner, M. 2005, AJ, in press
Weigelt, G., Balega, Y., Bloecker, T., et al. 1998, A&A, 333, L51
Weigelt, G., Balega, Y. Y., Blöcker, T., et al. 2002, A&A, 392, 131
Zuckerman, B., Dyck, H. M., & Claussen, M. J. 1986, ApJ, 304, 401